Dual-Mode Nanoprobes Based on Lanthanide Doped Fluoride Nanoparticles Functionalized by Aryl Diazonium Salts for Fluorescence and SERS Bioimaging

Huan Chen, Philippe Nizard, Philippe Decorse, Sophie Nowak, Souad Ammar-Merah, Jean Pinson, Florence Gazeau, Claire Mangeney, Yun Luo

To cite this version:

Huan Chen, Philippe Nizard, Philippe Decorse, Sophie Nowak, Souad Ammar-Merah, et al.. Dual-Mode Nanoprobes Based on Lanthanide Doped Fluoride Nanoparticles Functionalized by Aryl Diazonium Salts for Fluorescence and SERS Bioimaging. Small, 2023, ⟨10.1002/smll.202305346⟩. ⟨hal-04273637⟩

HAL Id: hal-04273637
https://hal.science/hal-04273637v1

Submitted on 8 Nov 2023

DOI: 10.1002/ ((please add manuscript number))
Article type: Full Paper

Dual-mode Nanoprobes Based on Lanthanide Doped Fluoride Nanoparticles Functionalized by Aryl Diazonium Salts for Fluorescence and SERS Bioimaging

Huan Chen[1,2], *Philippe Nizard*[1,4], *Philippe Decorse*[3], *Sophie Nowak*[3], *Souad Ammar-Merah*[3], *Jean Pinson*[3], *Florence Gazeau*[2 *], *Claire Mangeney*[1*], *Yun Luo*[1*]

1 Université Paris Cité, CNRS, Laboratoire de Chimie et de Biochimie Pharmacologiques et Toxicologiques, F-75006 Paris, France
2 Université Paris Cité, CNRS, Laboratoire Matière et Systèmes Complexes MSC, F-75006 Paris, France
3 Université Paris Cité, CNRS, ITODYS, F-75013 Paris, France
4 Structural and Molecular Analysis platform core facility of BioMedTech Facilities INSERM US36 | CNRS UAR2009 | Université Paris Cité

E-mail: yun.luo@u-paris.fr; claire.mangeney@u-paris.fr; florence.gazeau@u-paris.fr;

Keywords: Lanthanide doped fluoride nanoparticles, Aryl diazonium salts, Raman spectroscopy, Fluorescence, Bimodal imaging.

Abstract

The design of dual-mode fluorescence and Raman tags stimulates a growing interest for biomedical imaging and sensing applications as they offer the possibility to synergistically combine the versatility and velocity of fluorescence imaging with the specificity of Raman spectroscopy. Although lanthanide-doped fluoride nanoparticles (NPs) are among the most studied fluorescent nanoprobes, their use for the development of bimodal fluorescent-Raman probes has never been reported yet, to the best of our knowledge, probably due to the difficulty to functionalize them with Raman reporter groups. We fill this gap herein by proposing a fast and straightforward approach based on aryl diazonium salt chemistry to functionalize Eu^{3+} or Tb^{3+} doped CaF_2 and LaF_3 NPs by Raman scatters. The resulting surface-enhanced Raman spectroscopy (SERS)-encoded lanthanide-doped fluoride NPs retained their fluorescence labeling capacity and displayed efficient SERS activity for cell bioimaging. The potential of this new generation of bimodal nanoprobes was assessed through cell viability assays and intracellular fluorescence and Raman imaging, opening up unprecedented opportunities for biomedical applications.

1. Introduction

Dual-mode optical tags based on both fluorescence and Raman signals, gathered within a single probe, have attracted much attention in recent years as they hold great promise for biomedical imaging and sensing.[1] Such tags offer a unique combination of (i) fluorescence properties allowing high spatial and temporal resolution spectroscopy as well as fast imaging speed on wide surface area[2] and (ii) specific “fingerprint”-like Raman spectral signatures for multiplex Raman imaging.[3] However, due to the intrinsic inefficiency of the Raman process, the Raman signals of bimodal

Raman-fluorescence tags are very weak, which limits their applicability for bioimaging. To overcome this shortcoming, the fluorescence and Raman labels have been attached on plasmonic nanoparticles (NPs), such as gold or silver NPs, in order to take advantage of the huge enhancement of the local fields offered by these optically resonant metal NPs when they are excited in their localized surface plasmon resonances (LSPR).[1] This effect results in a strong amplification of (i) the Raman signal of scatterers located in the close vicinity of the metallic NPs surface, so-called surface-enhanced Raman scattering (SERS)[4] and (ii) the fluorescence signal of emitters separated from the metallic surface using spacers (such as silica layers or large molecules) to minimize quenching, so-called metal-enhanced fluorescence.[5] However, the design of such plasmon-based bimodal tags poses several practical challenges as it requires careful control over the distance between the fluorophore and the NPs surface to avoid non-radiative energy transfer.[6] Besides, plasmonic NPs exhibit a photothermal effect due to ohmic loss under laser excitation of LSPR, inducing local heating of the surrounding medium, with potential unwanted side effects in biological environments.[7] Non-plasmonic SERS substrates, such as carbon, silicon, oxide or chalcogenide NPs, have been proposed recently as interesting alternatives to plasmonic SERS tags to extend the range and versatility of optical labels.[8] In this case, the mechanism of Raman signal enhancement has been attributed to interfacial charge transfer between the NPs and the adsorbed scatters, called a chemical effect,[9] in contrast to the electromagnetic effect provided by plasmonic NPs. Non-plasmonic SERS substrates offer several advantages including their low cost, high chemical stability and biocompatibility combined with a minimization of plasmon-based side effects, such as localized heating and photocatalytic side reactions. However, they have never been used for bimodal SERS-fluorescence imaging up to now, to the best of our knowledge, probably due to the difficulty of combining intense and stable fluorescent probes with non-plasmonic SERS labels. We fill this gap herein by proposing a fast and straightforward approach to obtain innovative bimodal nanoprobes, based on the surface functionalization of fluorescent NPs by Raman scatters derived from aryl diazonium salts (see illustration in **Figure 1**). Fluoride NPs (CaF_2 and LaF_3) doped with europium and terbium lanthanide cations were selected for the fluorescent components of the bimodal nanoprobes due to their outstanding properties[10] such as low cytotoxicity,[11] tunable morphology and emission,[12] long luminescence lifetime,[13] large anti-stokes shift,[14] low photobleaching,[15] and high photostability.[15-16] Moreover, doped nanofluorides were shown recently to act as innovative nanotracers for in vivo ^{19}F MRI.[17] Aryl diazonium salts were selected as coupling agents for the attachment of Raman reporters on the fluorescent cores as they exhibit several advantages such as their ease of preparation, rapid grafting and large choice of reactive functional groups.[18] It is noteworthy that aryl diazonium salts have never been used for the surface functionalization of fluoride NPs. This proof-of-concept study thus offers new breakthroughs both for the surface engineering of CaF_2 and LaF_3 NPs and for the design of non-plasmonic bimodal SERS-fluorescence tags. Two aryl diazonium salts with different para-substituents ($-NO_2$, $-C\equiv N$) were used as Raman reporters. The choice of these diazonium salts was motivated by their characteristic spectral fingerprints ($-C\equiv N$ stretching mode at ~ 2200 cm^{-1} in the Raman-silent region and intense $-NO_2$ stretch peak at ~ 1330 cm^{-1}). The resulting SERS-encoded lanthanide doped fluoride NPs were characterized by UV-vis and fluorescence spectroscopies, Transmission Electron Microscopy (TEM), X-ray Diffraction (XRD), Dynamic Light Scattering (DLS), X-ray photoelectron Spectroscopy (XPS) and SERS. Their potential for bimodal imaging was then assessed through cell viability assays and intracellular fluorescence and Raman microscopies, demonstrating cutting edge capacity for biomedical applications.

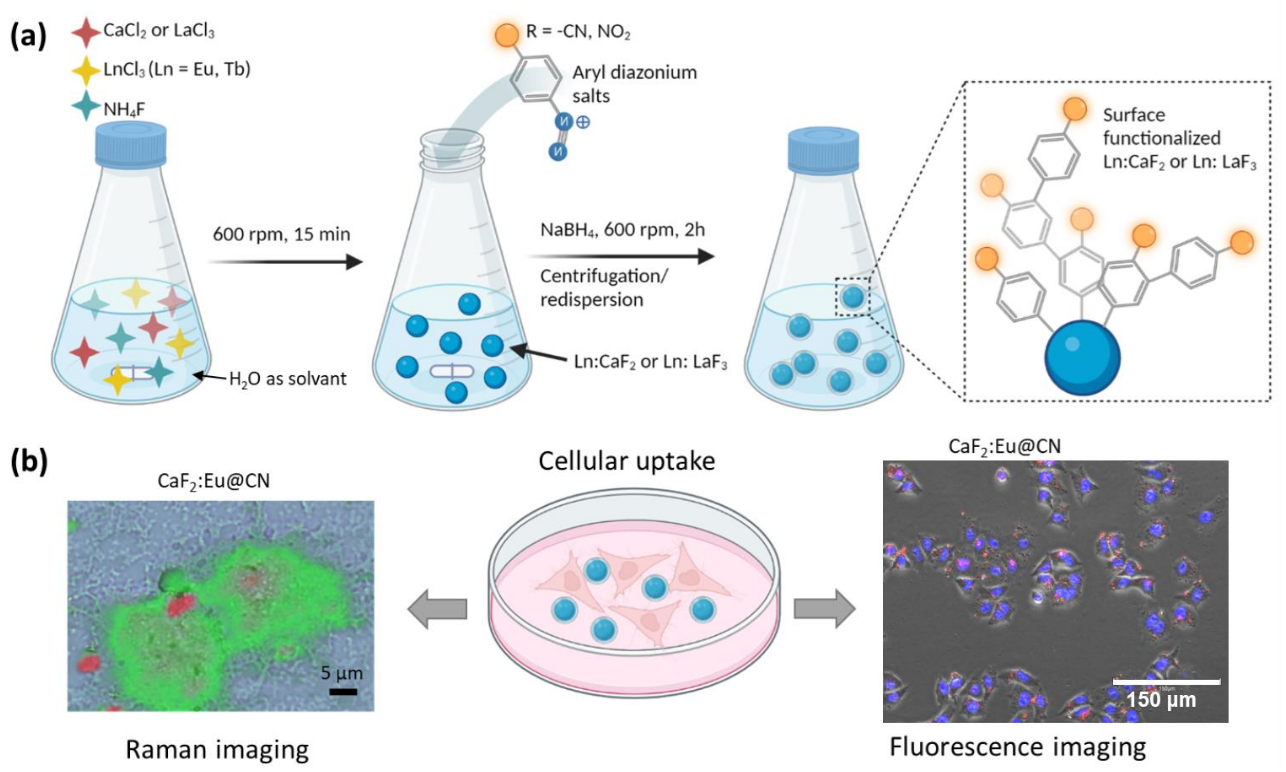

Figure 1. (a) Illustration of the elaboration and surface functionalization of lanthanide doped fluoride NPs (CaF_2:Eu, CaF_2:Tb, LaF_3:Eu and LaF_3:Tb) by aryl diazonium salts (with $–NO_2$ or –CN groups) and (b) use of the resulting bimodal nanoprobes for Raman (left) and fluorescence (right) cell imaging. Created with BioRender.com.

2. Results and Discussion

2.1. Synthesis of the bimodal nanoprobes and characterization

The synthesis of the bimodal nanoprobes was performed in two steps: (1) the elaboration of the nanoscale luminescent building blocks; (2) the immobilization of Raman reporters on their surface. In the first step, doped fluoride NPs were synthesized using a co-precipitation method slightly adapted from the literature[19] (see details in the experimental section in supporting information), yielding CaF_2 and LaF_3 NPs doped with either Eu or Tb and named CaF_2:Eu, CaF_2:Tb, LaF_3:Eu and LaF_3:Tb. The TEM images revealed the formation of NPs with mean sizes in the range 13-16 nm (see **Figure 2**, **Figure S1** and **Table 1**).

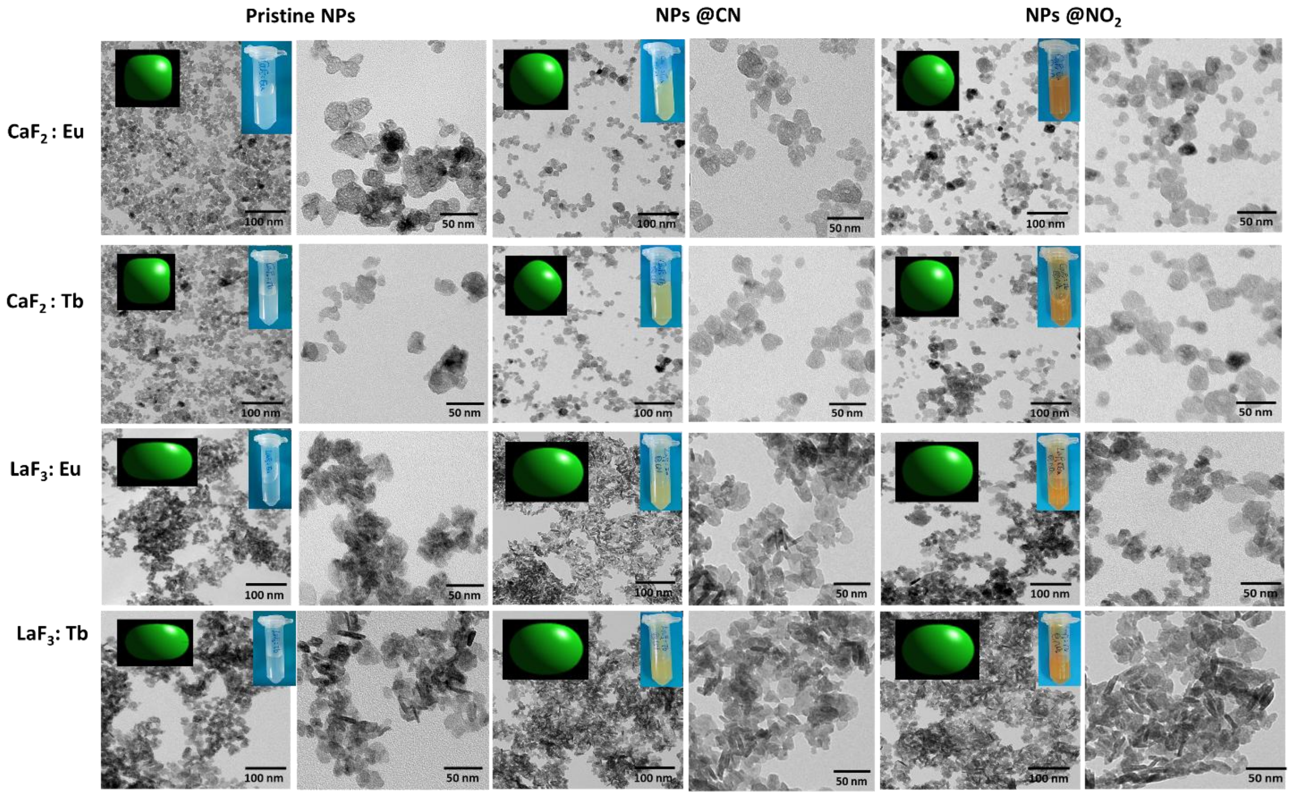

Figure 2. TEM images of CaF$_2$:Eu, CaF$_2$:Tb, LaF$_3$:Eu and LaF$_3$:Tb NPs, before (pristine NPs) and after functionalization by aryl diazonium salts bearing either –CN (NPs@CN) or –NO$_2$ (NPs@NO$_2$) Raman reporter groups. Optical pictures of the NPs dispersions after washing are provided next to the TEM pictures of each sample together with the shape of the crystallites (in green) obtained from the MAUD software. It is noteworthy that the sizes of the crystallites in these images have been adjusted for the sake of clarity but they are not proportionate to the sizes deduced from the MAUD software.

The XRD patterns recorded for all the calcium-based produced powders (**Figure S2**) were found to be similar one to another. The same feature was observed for the ones recorded for lanthanum-based NPs, the former matching very well with the expected fluorite (Fm3m space group) structure and the latter with the rhombohedral (P-3c1 space group) structure. Focusing on the position of the main peak of each pattern series, a net shift to higher 2θ values can be nevertheless observed in the pattern of the doped samples compared to non-doped ones, in agreement with the partial replacement of Ca^{2+} or La^{3+} into the fluoride crystallographic lattices by the lanthanide Eu^{3+} and/or Tb^{3+} cations. Rietveld refinements were performed, thanks to MAUD software[20] on all the collected data and allowed to determine the shape and size of the crystallites for each phase. A cubic shape with 13-14 nm sides was obtained for CaF_2 NPs. In contrast, the LaF_3 NPs exhibit an anisotropic oblate shape characterized by a polar axe of *ca.* 4 nm in the (00l) crystallographic direction and an equatorial length of *ca*. 9 nm in the (h00) direction (see more details in **Table 1**). These values are in line with the average NPs sizes estimated by TEM for doped and non-doped CaF_2 NPs. However, there is a discrepancy between the values obtained by XRD and TEM for LaF_3 NPs, suggesting some degree of aggregation. The DLS data (**Table 1**) confirmed some degree of NPs aggregation, particularly for LaF_3 NPs, with hydrodynamic diameters in water lying in the range 66-229 nm.

Table 1. Summary of the NPs and crystallite sizes determined from TEM, DLS and XRD. The given errors represent standard deviations.

Samples	Mean particle size from TEM (nm)	Hydrodynamic size from DLS (nm)	PDI [a]	Crystallite size from XRD (nm)
CaF_2:Eu	13 ± 1	86 ± 34	0.15	Cube of 13 nm side
CaF_2:Tb	15 ± 1	66 ± 18	0.07	Cube of 14 nm side
LaF_3:Eu	13 ± 2	166 ± 74	0.20	Oblate 4 x 9 nm
LaF_3:Tb	15 ± 2	131 ± 58	0.19	Oblate 4 x 9 nm
CaF_2:Eu@CN	16 ± 2	66 ± 24	0.13	18 nm average
CaF_2:Eu@NO_2	16 ± 2	88 ± 42	0.20	18 nm average
CaF_2:Tb@CN	16 ± 2	72 ± 28	0.16	19 nm average
CaF_2:Tb@NO_2	16 ± 2	76 ± 20	0.07	17 nm average
LaF_3:Eu@CN	16 ± 2	78 ± 18	0.05	Oblate 11 x 16 nm
LaF_3:Eu@NO_2	16 ± 2	80 ± 22	0.07	Oblate 11 x 15 nm
LaF_3:Tb@CN	16 ± 2	76 ± 34	0.19	Oblate 11 x 15 nm
LaF_3:Tb@NO_2	16 ± 2	72 ± 26	0.12	Oblate 11 x 15 nm

[a] PDI (polydispersity index) obtained from DLS

The aryl diazonium salts (4-nitrobenzenediazonium tetrafluoroborate or 4-cyanobenzenediazonium tetrafluoroborate, final concentration 10^{-2} mol.L^{-1}) were first synthesized (see details in SI) and then added to the aqueous NPs colloidal solution ([NPs] = 1 mg·mL^{-1}) in the presence of a reducing agent ($NaBH_4$, 2.4×10^{-2} mol·L^{-1}). The reaction was carried out at room temperature during 2 h. The obtained yellow and brown dispersions were washed by 3 cycles of centrifugation/redispersion in water, and the resulting NPs were named CaF_2:Eu@CN, CaF_2:Tb@CN, CaF_2:Eu@NO_2, CaF_2:Tb@NO_2, LaF_3:Eu@CN, LaF_3:Tb@CN, LaF_3:Eu@NO_2, or LaF_3:Tb@NO_2 depending on the lanthanide dopant (Eu or Tb) and functional group (-CN or –NO_2) carried by the diazonium salt used for the reaction. The TEM images didn't reveal any significant modification of the NPs shape, structure and size after functionalization (**Figure 2** and **Figure S2**). However, the diffraction patterns revealed a slight increase in the crystallite sizes (see **Table 1**) after functionalization and some modifications of their shapes, particularly for the CaF_2 based particles which become nearly-spherical with a blunt cube shape, suggesting partial dissolution and recrystallization in a kind of a ripening. In contrast, the DLS analysis indicated a general decrease of the hydrodynamic diameters of LaF_3 NPs, which could be explained by a disintegration of the pre-existing clusters, improving the colloidal stability of the primary particles after functionalization by the aryl diazonium salts. The surface chemistry of the fluoride NPs was analyzed by XPS. As observed in **Figure 3**, the XPS survey spectra of the pristine NPs display intense peaks related to Ca 2p (at *ca.* 348 eV) for CaF_2, La 3d (at *ca.* 836 eV) for LaF_3 and F 1s (at *ca.* 685 eV) for both NPs.

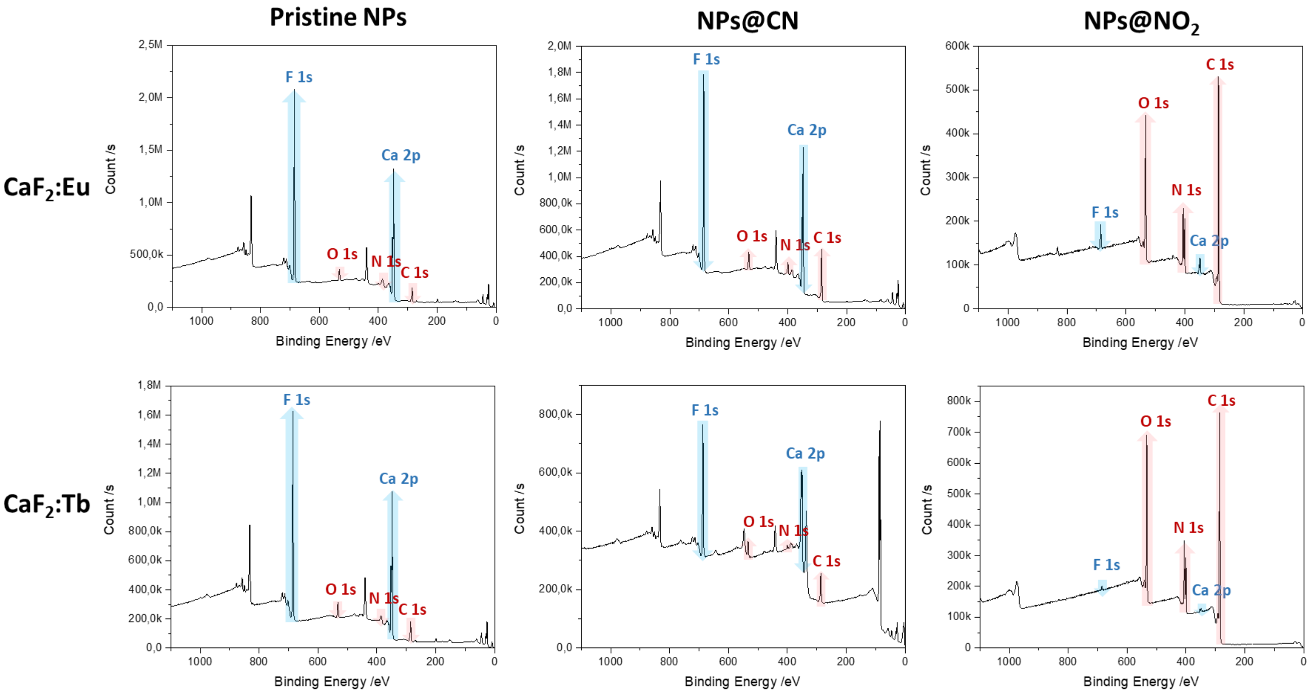

Figure 3. XPS survey spectra of the pristine doped fluoride NPs (CaF_2:Eu, CaF_2:Tb, LaF_3:Eu and LaF_3:Tb) and the NPs functionalized by the two diazonium salts, bearing either $–NO_2$ or CN moieties. It is noteworthy that the intense peaks detected at 84 and 336 eV for CaF_2:Tb@CN are due to the underlying gold surface on which the powders were deposited.

The relative intensities of these peaks are in good agreement with the CaF_2 and LaF_3 structures, with twice F content (54-56 %) compared to Ca (27.-28 %) for CaF_2, and around three times more F (57-64 %) compared to La (17-21 %) for LaF_3 NPs. The Eu and Tb dopants could also be detected at *ca*. 1150 eV (Eu 3d signal) and 1250 eV (Tb 3d signal). However, as XPS is a surface sensitive technique, the intensity of these signals is very low (less than 1 at.%) due to their loading within the NP cores. The surface elemental compositions of all samples are summarized in **Table 2**. Interestingly, important modifications were observed on the survey spectra after functionalization by the diazonium salts, with a strong attenuation of the Ca/La and F signals while the carbon, nitrogen and oxygen contents sharply increased. These evolutions of the surface elemental compositions confirm the coating of the fluoride NPs by organic layers.

Table 2. Surface chemical composition (atom%) of doped CaF_2 and LaF_3 NPs before and after functionalization by the diazonium salts bearing either NO_2 or CN groups, as determined by XPS analysis.

Samples	**Ca**	**La**	**Eu**	**Tb**	**F**	**C**	**O**	**N**
Eu and Tb doped CaF_2 NPs								
CaF_2:Eu	28.1	-	1.0	-	56.4	8.5	5.4	0.6
CaF_2:Tb	27.2	-	-	0.9	54.5	11.4	5.6	0.4
CaF_2:Eu@CN	19.5	-	0.5	-	36.6	33.1	4.0	6.3
CaF_2:Tb@CN	20.8		-	0.6	40.8	30.1	5.5	2.2
CaF_2:Eu@NO_2	1.4	-	-	-	2.5	62.9	16.4	16.8
CaF_2:Tb@NO_2	0.2	-	-	-	0.5	64.6	17.1	17.6
Eu and Tb doped LaF_3 NPs								
LaF_3:Eu	-	20.8	1.1	-	63.7	10.6	3.7	-
LaF_3:Tb	-	17.6	-	-	57.1	19.1	6.2	-
LaF_3:Eu@CN	-	8.3	-	-	29.8	42.8	10.0	9.0
LaF_3:Tb@CN	-	13.0	-	-	40.5	30.5	10.9	5.1
LaF_3:Eu@NO_2		15.6			49.2	24.2	9.4	1.6
LaF_3:Tb@NO_2		4.2			14.1	49.6	18.3	13.9

It is noteworthy that the oxygen signal of the bare fluoride NPs displays two peaks, one at 531.5 eV, assigned to some O^{2-} species, and the other one at 533.2 eV that is associated to some surface OH^- groups, as already described elsewhere.[21] Surprisingly, the nitrogen content appears superior to the value expected for pure nitro or cyano-polyaryl layers. Based on the high resolution N 1s spectra (see **Figure** 4 for CaF_2 NPs), it appears that 2 components can actually be detected: for CaF_2:Ln@NO_2, a peak is observed at 405.4 eV, which is related to the NO_2 groups while for CaF_2:Ln@CN, a peak is observed at 399.0 eV, related to C≡N groups. In addition to these characteristic signals, another component is detected in both types of samples, at 400 eV, which can be attributed to the presence of azo groups (N=N) [22]. The presence of this component suggests that surface functionalization occurs, at least partly, via azophenyl radical pathways, as already reported in other studies.[22a, 23] These XPS data thus indicate that the polyaryl coating around the NPs contains both Ar-Ar and Ar-N=N-Ar bonds.

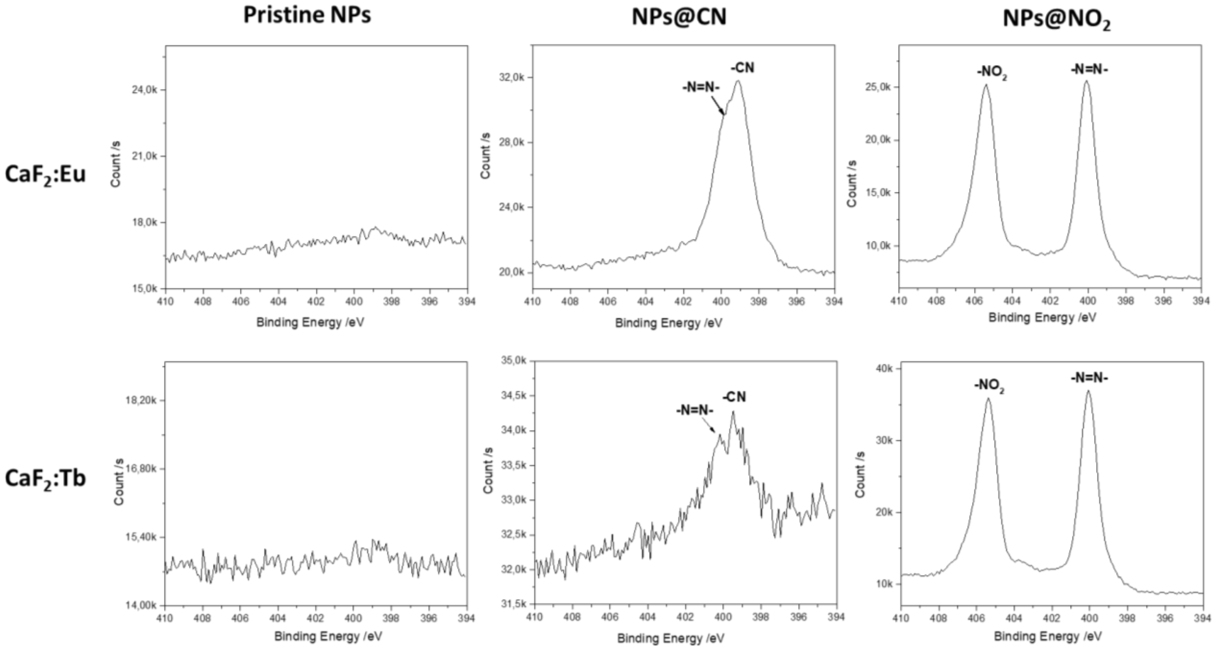

Figure 4. XPS high resolution N 1s spectra of the pristine doped CaF_2 NPs (CaF_2:Eu, CaF_2:Tb) and the NPs functionalized by the two aryl diazonium salts, bearing either –NO_2 or CN moieties.

The fluoride NPs were also examined by ATR-FTIR. The strong peak observed at ~ 3250-3260 cm^{-1} in the IR spectra of the unmodified NPs (see IR spectrum of CaF_2:Eu in **Figure S3**) confirmed the presence of OH surface groups, in agreement with the XPS analysis. Some residual NH_4F was also detected between ~1000 and 1600 cm^{-1}. After reaction with the diazonium salt bearing CN moieties, the IR spectra was strongly modified with the appearance of the characteristic vibrations of the aromatic ring at 1600 cm^{-1} and the CN group at 2227 cm^{-1}. All together, these spectra confirm the expected functionalization of the NPs.

2.2 Optical properties of the bimodal nanoprobes

The optical properties of the bimodal nanoprobes were studied using fluorescence and Raman spectroscopies. The photoluminescence of Eu doped fluoride NPs (**Figure 5**) exhibits distinct emission peaks at 597 nm, 620 nm and 701 nm, related to $^5D_0 \rightarrow {}^7F_j$ (j = 1, 2, 4) transitions, characteristic of Eu doping in CaF_2 and LaF_3 lattices.[24]

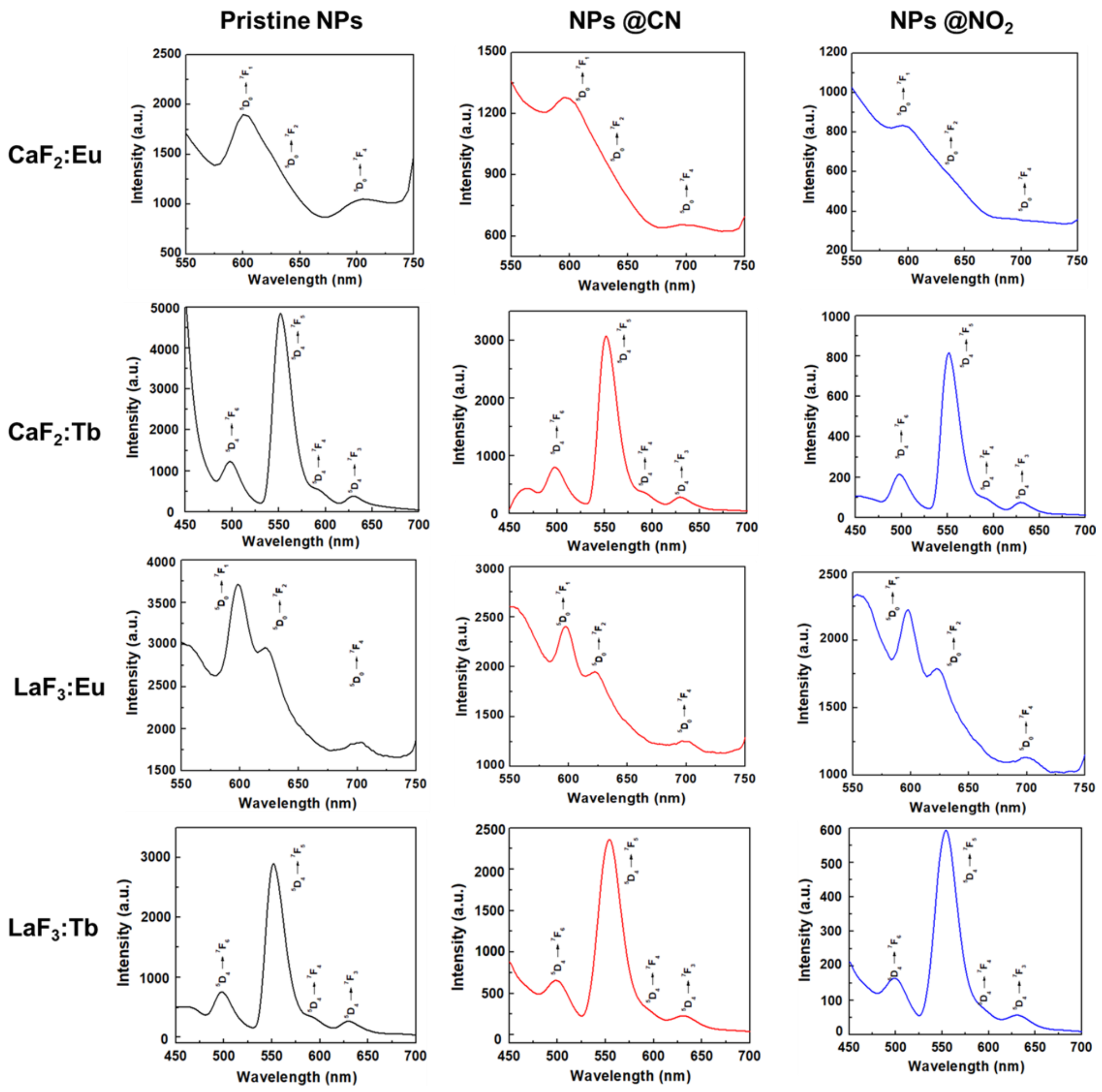

Figure 5. (a) Photoluminescence spectra of aqueous dispersions of Eu and Tb-doped fluoride NPs (at 5 mg mL^{-1}), λ_{ex} = 420 nm for Tb and 395 nm for Eu.

For Tb doped NPs, the emission peaks appear at 497 nm, 551 nm, 592 nm and 629 nm, related to $^5D_4 \rightarrow {}^7F_j$ (j = 6, 5, 4, 3) transitions. As evident from **Figure 5**, the fluorescence intensity of doped fluoride NPs slightly decreases after surface functionalization. This quenching effect can be explained by some non-radiative decay caused by multi-phonon relaxation processes and vibrational deactivation from surface-bound ligands, as already reported in the literature.[25] Indeed, compared to their bulk counterparts, lanthanide-doped NPs generally undergo stronger surface quenching effects due to their high surface-to-volume ratio, which favors the presence of a large portion of dopant ions on the outermost layer of the NPs, leading to surface-related energy-loss mechanism. Moreover, the polyaryl coating exhibits an absorption band around 400 nm (see **Figure S4**), coinciding with the excitation wavelength (λ_{ex} = 420 nm), which may also contribute to the fluorescence intensity decrease. However, the fluorescence intensity of the functionalized NPs remains high enough to enable fluorescent labeling of cells, as detailed later.

The SERS signals of the functionalized fluoride NPs were recorded on dried drops at 638 nm laser excitation and compared to the Raman spectra of the free diazonium salt powders (**Figure 6**). The characteristic N≡N stretching peak of the diazonium salt powders, detected at *ca.* 2280-2300 cm^{-1} (yellow cage in **Figure 6**), vanishes after the functionalization of the fluoride NPs. This observation is in agreement with the grafting reaction mechanism based on the formation of aryl radicals by reduction of the aryl diazonium salts and loss of $-N_2^+$. The formed aryl radicals are very reactive and are thus expected to bind to the fluoride NPs surface and to the already grafted aromatic groups *via* homolytic aromatic substitution, leading to polyaryl coatings.[26] The SERS spectra of the functionalized fluoride NPs confirm this mechanism with the appearance of the characteristic signature of phenyl-derivatives stemming from diazonium salts, including peaks at *ca.* 1580-1595 cm^{-1} (ortho-meta C=C stretching mode) and 1135 cm^{-1} (CH in plane bending).[18g, 22b, 26-27] In addition, the stretching modes of the Raman reporter groups (-NO_2 and -CN) are well detected at 1330 cm^{-1} and 2220 cm^{-1}, respectively. It is noteworthy that the bare unfunctionalized doped fluoride NPs exhibited no Raman signature in the spectral region 500-2500 cm^{-1} (see **Figure S5**).

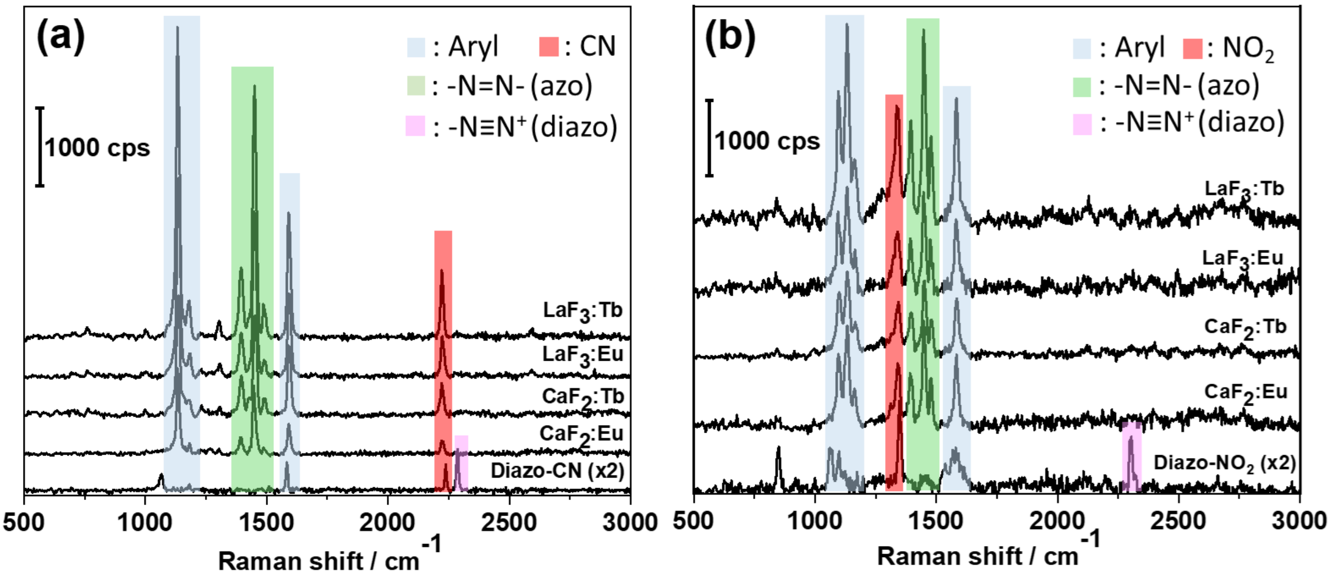

Figure 6. SERS spectra of doped fluoride NPs functionalized with the diazonium salts bearing (a) -CN groups and (b) -NO_2 groups. The Raman signals of the parent aryl diazonium salts (pure powders) are also provided for the sake of comparison, with intensity × 2. The blue, green, pink and red cages refer to the vibrational modes of aryl, -N=N-, N_2^+ and Raman tags (CN or NO_2), respectively. The excitation wavelength λ was 638 nm and exposure time 2s.

Interestingly, new peaks related to the presence of diazenyl groups within the polyaryl coating were also clearly detected at *ca.* 1395, 1450 and 1480 cm^{-1}.[28] This observation confirms that azo coupling reactions, based on the electrophilic attack of the diazonium cation on the already grafted aromatic rings, are also involved in the growth of the polyaryl layers at the surface of the fluoride NPs, through −Ph−N=N−Ph−R linkages, in line with G. Deniau et al.[22a] These results demonstrate that diazonium salt chemistry offers an easy means to functionalize fluoride NPs. The NO_2- and CN-coated NPs showed strong and uniform Raman response. The similarity of the SERS signals obtained on the different types of fluoride NPs emphasizes the high specificity of the functional polyaryl Raman signature, which is completely independent of the chemical nature of the cores (CaF_2 or LaF_3, Eu or Tb dopants). This specificity is a key feature for the design of SERS tags for cellular imaging applications. The chemical stability of the polyaryl-coated doped fluoride NPs was evaluated by monitoring the fluorescence and SERS signals in aqueous solutions of CaF_2:Tb@CN and CaF_2:Tb@NO_2 NPs over a period of up to 5 days, starting from just after their synthesis. Within this timeframe, slight aggregation of the NPs was noticed through DLS, leading to intensity fluctuations in both fluorescence and SERS signal intensity over time. Nevertheless, it is noteworthy that the overall spectral profile of the nanoprobes remained unaltered (as depicted in **Figure S6**), providing evidence of the chemical robustness of the polyaryl-coated doped fluoride NPs.

2.3. Cytotoxicity assessment of the bimodal nanoprobes

The cytotoxicity of the bimodal nanoprobes was assessed on HeLa cell lines, using an AlamarBlue assay. As observed in **Figure 7a-d**, 24 hours of incubation with NPs in complete culture medium did not affect the cell viability of HeLa cells even at the higher concentration (200 µg/ml) demonstrating the good biocompatibility of the bimodal nanoprobes.

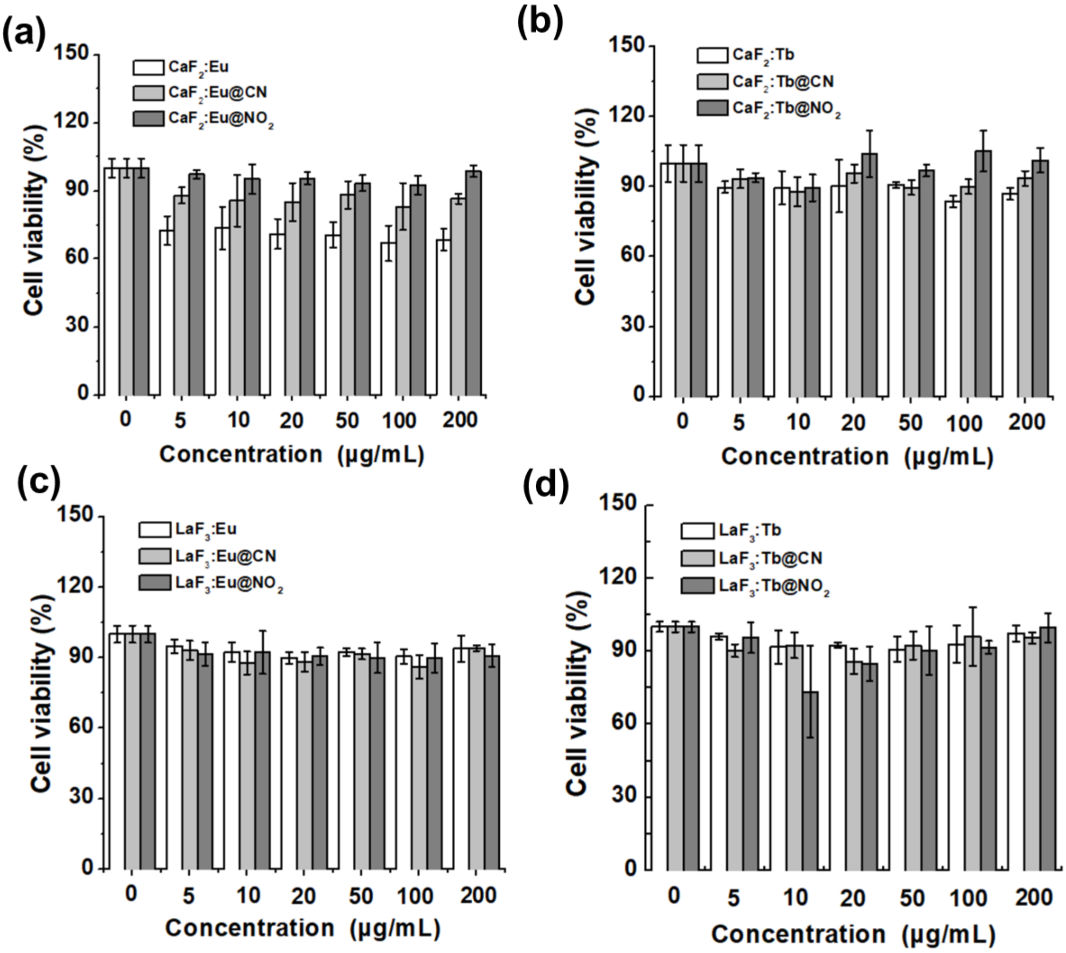

Figure 7. Cell viability assessment using AlamarBlue assay : HeLa cells were incubated for 24 hours with the pristine and functionalized fluoride NPs, at 7 different concentrations (from 0 to 200 μg.mL^{-1}) for 24 h. (a) CaF_2:Eu, CaF_2:Eu@CN, CaF_2:Eu@NO_2; (b) CaF_2:Tb, CaF_2:Tb@CN, CaF_2:Tb@NO_2; (c) LaF_3:Eu, LaF_3:Eu@CN, LaF_3:Eu@NO_2; (d) LaF_3:Tb, LaF_3:Tb@CN, LaF_3:Tb@NO_2.

2.4 Fluorescence imaging of HeLa cells after uptake of the bimodal nanoprobes

The fluorescent properties of the bimodal nanoprobes were exploited for cell fluorescence imaging experiments. HeLa cells were incubated for 24 hours with the various NPs, washed three times and fixed before confocal imaging with a CellInsight CX7^{TM} high content analysis microscopy platform. As observed in **Figure 8, t**he Eu and Tb fluorescence signals are distributed as bright spots in the cytoplasm of cells, likely corresponding to vesicular, endosomal and lysosomal compartment localization of the NPs.

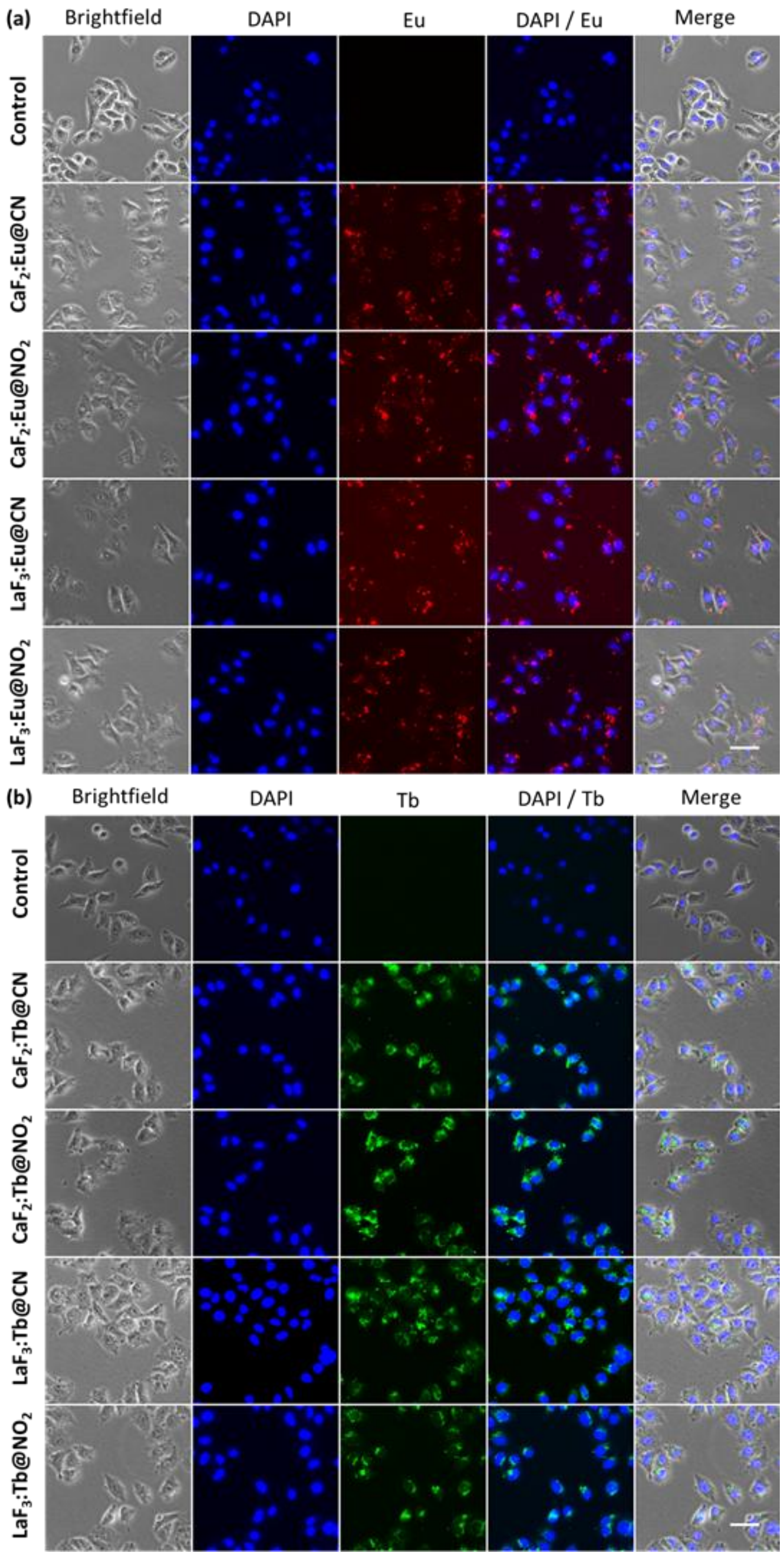

Figure 8. Brightfield, fluorescence and merge images of HeLa cells stained with DAPI (4’,6-diamidino-2-phenylindole, blue fluorescence) after incubation for 24h (or not for the control) with the bimodal nanoprobes (a) Eu-doped fluoride NPs and (b) Tb-doped fluoride NPs. Scale bar = 50 µm.

2.5 Raman imaging of HeLa cells after uptake of the bimodal nanoprobes

The bimodal nanoprobes were then used for Raman imaging experiments on HeLa cells. The NPs were first introduced in the cell culture medium, and after 6 h incubation, the free NPs were removed by gently washing the cells with media. The HeLa cells were then fixed, rinsed, and dried on a sample holder (glass slide) before analysis using Raman confocal microscope. As shown in **Figure 9**, the SERS signals of the nanoprobes (red and blue spots for –CN and –NO_2 labelled NPs, respectively) were not evenly distributed throughout the entire cells and could be easily distinguished from that of cells (green region) and sample holder (black area).

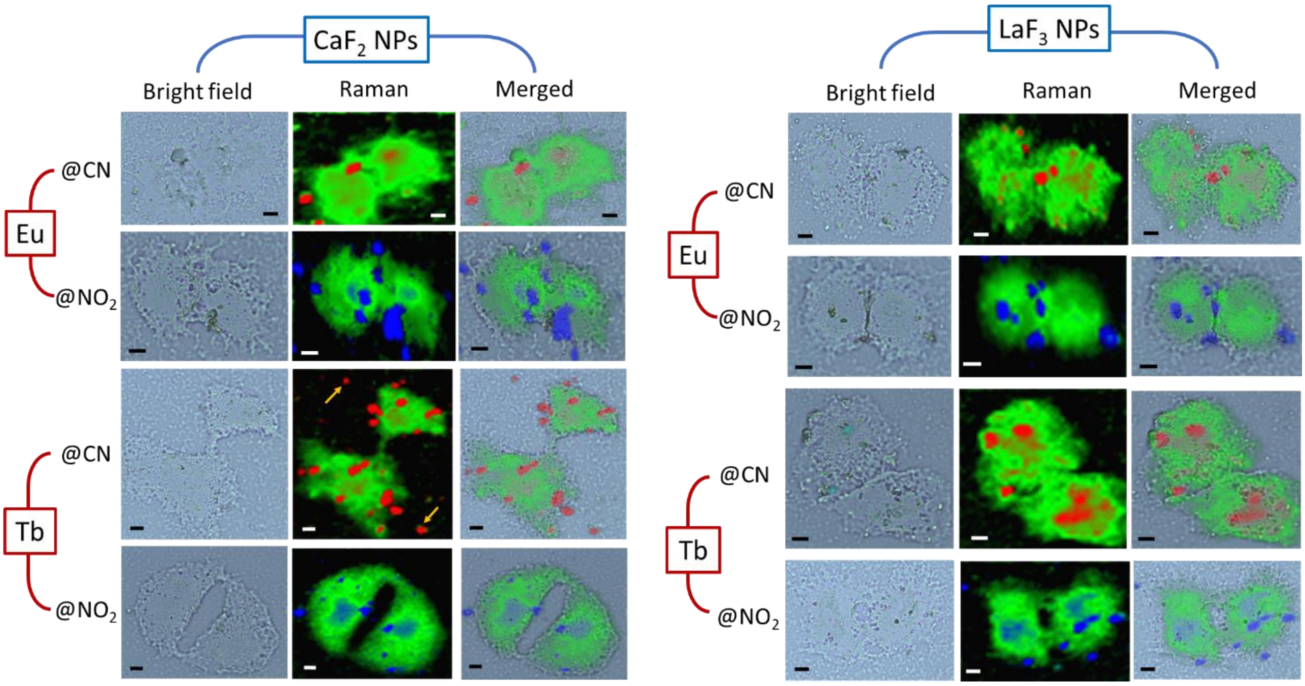

Figure 9. Bright field, Raman and merged optical/Raman images of HeLa cells after incubation with the bimodal NPs for 6 h. Scale bar = 5µm. The chosen color code for Raman imaging is the following: green for the Raman signal of cells, black for the sample holder (glass slide), red for the NPs@CN, and blue for the NPs@NO_2. Classical least square (CLS) fitting was employed for Raman maps, using average spectra collected from cell area, sample holder and nanoprobes as references (see **Figure S7**). The yellow arrows in sample CaF_2:Tb@CN refer to the signals of NPs detected outside the cells.

The average spectra of the red, blue, green and black regions observed on the Raman map are shown in **Figure S7.** The green one was assigned to the cell signals due to the lipid peaks observed in the 2800-3000 cm^{-1} region while the black region, with no detectable Raman signal was related to the sample holder. The spectrum profile of the red and blue regions is dominated by the signals of the Raman probes (-CN and $–NO_2$ respectively) but the peaks from the cell lipids are also visible. Interestingly, the cell Raman maps (in green) after NPs uptake (blue or red colors) can be perfectly overlaid with the cell optical images (see merged channel in **Figure 9a**), enabling the localization of NPs within the cells and around. In most cases, NPs seem located inside the cells but occasionally, red and blue signals are detected outside the cells (see yellow arrows in **Figure 9)**. The Raman spectra emanating from these nanoprobes detected outside the cells (refer to **Figure S8**) exhibit distinct signals characteristic of both the nanoparticles and the cells (notably lipid peaks), implying that they are probably located within cell fragments from deceased cells that have adhered to the substrate. It is noteworthy that the Raman signals of the presumably intracellular NPs are very similar to the Raman signal of the free or extracellular NPs (see **Figure S9**), emphasizing the high stability of the polyaryl coating derived from the diazonium salts around the NPs, even in the intracellular compartments after 6h uptake.

The 3D distribution of the bimodal NPs inside the cell was examined with high-resolution confocal Raman microscopy focusing on obtaining spatial information in x, y, and z directions in order to confirm their intracellular localization (see **Figure 10a** recorded after uptake of CaF_2: Eu@CN). One cell was scanned over a volume of $43 \times 55\times 8$ µm^3 (scan step of $0.6 \times 0.6 \times 1$ µm^3) with an acquisition time of 1 s per step (objective 100 x, 638 nm laser, 2 mW) and a series of slices (in z-direction) was imaged (see **Figure 10a**). For the top layer of the cell, the SERS signal mainly arises from the cell lipid peaks (green area) with almost no signal from the nanoprobes. Interestingly, the intensity of the nanoprobe signal (red signal) gradually increased for the deeper layers (towards the bottom of the cell, which is adherent to the substrate), confirming their internalization within the cell in line with intracellular Eu and Tb fluorescence detection. It is noteworthy that the signal of the nanoprobe was not found to be affected by their internalization, as their spectral fingerprint in the cell remained very similar to that of the nanoprobe before incubation (see **Figure 10b**). The 3D reconstruction image displayed in **Figure 10c** evidences the presence of the nanoprobes (red signal) within the cell (green signal), emphasizing the excellent cell uptake and Raman contrast ability of the diazonium salt-functionalized nanoprobes.

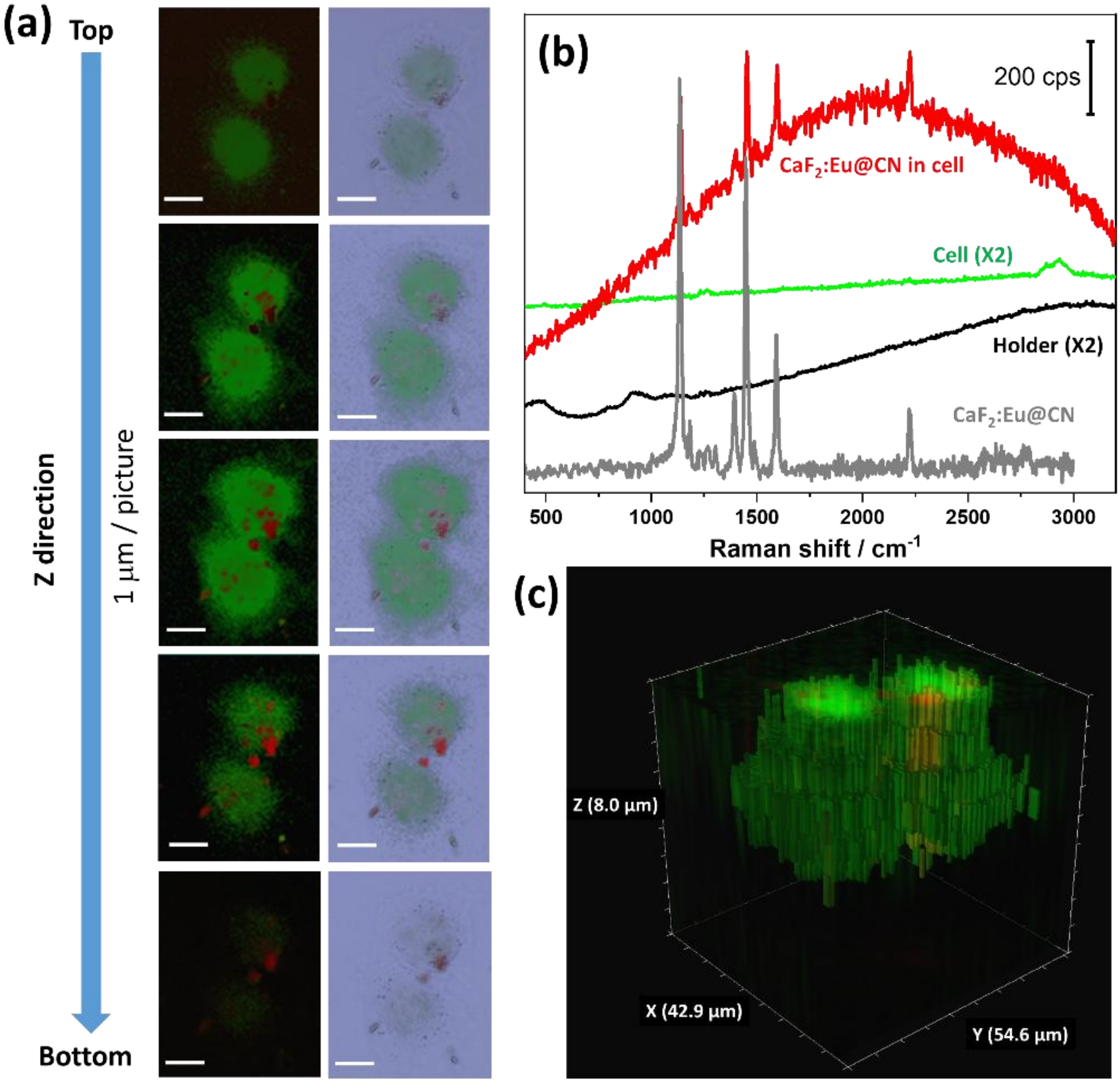

Figure 10. 3D confocal Raman imaging of a HeLa cell after incubation with CaF_2: Eu@CN nanoprobes. (a) Z-stack from the top to the bottom of the cell (analyzed by CLS fitting, see reference spectra in b), showing the distribution of the nanoprobes within the cell. The corresponding merged optical/Raman images are displayed on the right-hand side. Scale bar = 10 µm. (b) Representative SERS spectra of the nanoprobe within the cell (red curve) and comparison with the signal recorded outside the cell (grey curve). The typical spectra collected in cell (green curve, amplified by 2-fold) and background (sample holder, amplified by 2-fold) were also presented. (c) 3D reconstruction image based on the Z-stack scans.

3. Discussion

The key advantages of this surface functionalization strategy based on aryl diazonium salts are its simplicity, rapidity, and the use of environmentally friendly reaction conditions, *i.e.* in water at room temperature and in the presence of air. Regarding the mechanism of surface grafting on the fluoride NPs, some assumptions can be made. First, as fluoride is monovalent, attachment of the polyaryl layers to the NPs via the surface F atoms can be ruled out. Second, if the aryl radicals formed by the addition of the reducing agent ($NaBH_4$) reacted on CaF_2 or LaF_3 NPs by halogen atom abstraction,[29] one should obtain Ca or La-C_6H_4-NO_2/CN. In this case, the XPS data should exhibit a C1s contribution at low energy (around 283-284 eV) as the electronegativity of Ca (EN = 1.0) and La (EN = 1.1) are much lower than that of carbon (EN = 2.5). As such a peak is absent from the C1s signal of the functionalized NPs, this possibility can be also ruled out. Another possibility would be the abstraction of a F atom by the aryl radicals to give F-C_6H_4-NO_2/CN that would remain adsorbed on the NPs surface. In this case, the XPS C1s component would be characterized by a distinct component at ca. 288 eV,[30] which is not observed in the XPS spectra of the functionalized NPs. As the analysis of the pristine fluoride NPs by XPS and ATR-FTIR reveals the presence of surface OH groups (XPS O1s component at *ca.* 534 eV[21] and IR peak at ~ 3250 cm^{-1}), we propose that the attachment of the aryl radicals takes place on these OH groups, as already observed on other types of oxidized surfaces, such as CuO,[31] CeO_2, MnO_2 and Fe_2O_3.[32] In this case, the bonding would rely on Ca/La-O-C bonds and the signature of C-O bonds should be present in the XPS spectra; a contribution is indeed observed at ~286 eV in the spectra of the functionalized NPs that could be related to the C-O components. It is noteworthy that this component is also associated with the presence of C-N bonds in the coating. The proposed grafting mechanism is summarized in **Figure 11**. $NaBH_4$, known for its ability to provide hydride ions, reduces the diazonium salt resulting in the formation of the corresponding aryl radical[33]. This aryl radical then abstracts a hydrogen atom from one of the OH groups present on the CaF_2 or LaF_3 NP surface generating an oxygen radical; coupling of the aryl radical with the oxygen radical terminates the reaction to give the aryl substituted nanoparticles[32a, c]

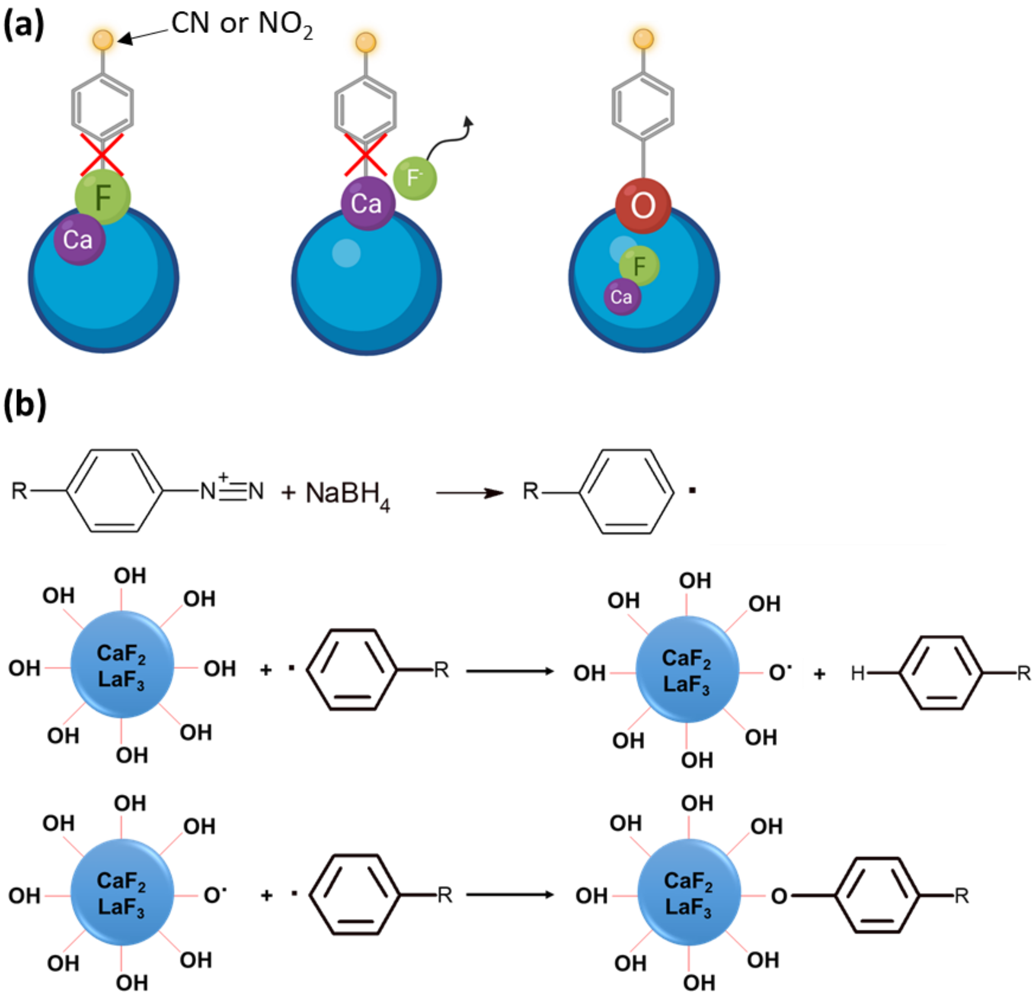

Figure 11. (a) Illustration of surface functionalization of fluoride NPs by aryl diazonium salts. The experimental results support the formation of Ca/La-O-C bonds on the NPs surface instead of direct grafting *via* F-C or Ca/La-C bonding. Created with Biorender. (b) Summary of the proposed grafting mechanism based on the reduction of the diazonium salts by $NaBH_4$ to give the corresponding aryl radicals. The formed radical abstracts a hydrogen atom from one of the OH groups of the CaF_2 or LaF_3 NPs to give an oxygen radical, which further reacts with an aryl radical to give the aryl substituted nanoparticles.

Regarding the optical properties of the functionalized doped nanoprobes, they demonstrate efficient labeling capacity for cell fluorescence imaging, despite a small decrease in the fluorescence intensity due to some quenching effect induced by the surface-bound ligands. The nanotags could also be used for cell Raman imaging with intense SERS signals. Remarkably, the spectral fingerprint remained very similar after internalization within the cell to that before incubation, demonstrating the high stability of the polyaryl coating attached to the NPs' surface in a biological environment. An estimation of the SERS Enhancement Factor (EF) provided by the immobilization of the Raman reporter groups on the NPs surface was performed by comparing their Raman signal intensities in the presence or absence of the fluoride NPs (see details of the experiments in SI, as well as **Figure S10**). The calculation of EF was performed only on fluoride NPs@CN nanoprobes as the nitro signal of NPs@NO_2 was found unstable under the experimental conditions used for the determination of EF, probably due to some photodegradation reactions. The obtained EF was found in the range 2-70 (**Figure 12**), depending on the peak considered for the calculation (aryl at *ca.* 1590 cm^{-1} or CN at 2220 cm^{-1}) and the initial diazonium salt concentration. Higher diazonium salt concentrations were associated with lower EF, which can be explained by the presence of thick polyaryl coatings around the NPs, minimizing the surface enhancement contribution in the overall Raman signal. In contrast, in the presence of thin polyaryl layers (obtained at low initial concentrations of diazonium salts), the surface enhancement effect is predominant in the Raman signal. Such Raman EF combined with the fluorescent characteristics of the nanoprobes appears as a valuable feature for cell bimodal imaging experiments.

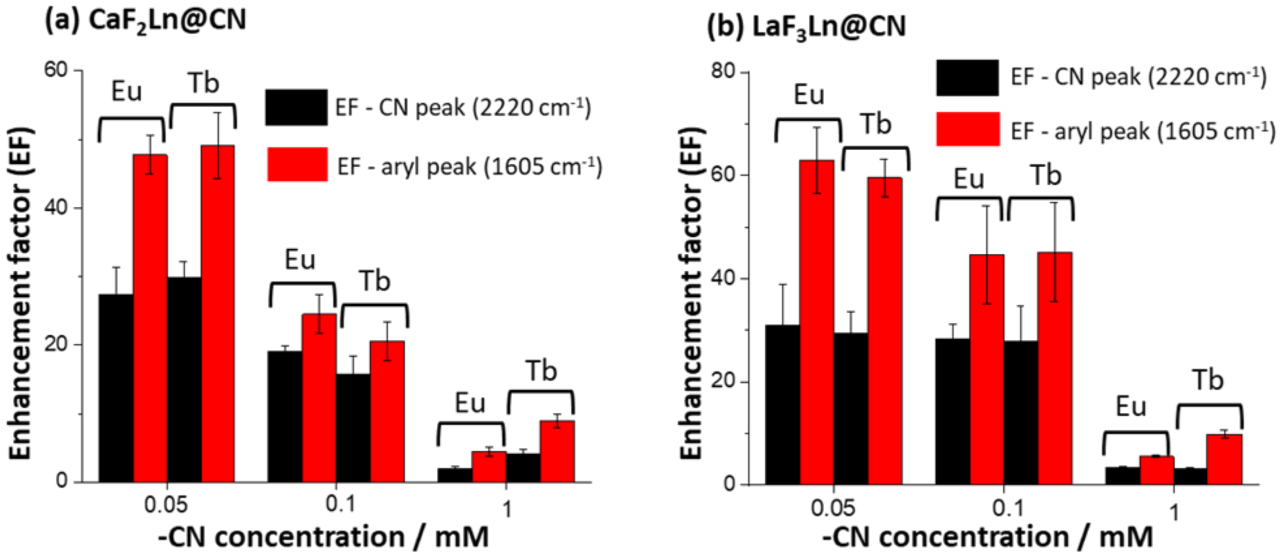

Figure 12. SERS enhancement factors (EF) calculated on doped fluoride NPs@CN, using the –CN or –aryl peak intensities compared to the parent polyaryl layers (in absence of NPs). The EF values were calculated using various initial concentrations of aryl diazonium salt (0.05, 0.1 and 1 mM).

4. Conclusion

In summary, the surface functionalization of lanthanide-doped fluoride NPs by aryl diazonium salts bearing Raman labels appears promising to obtain a new generation of bimodal SERS encoded-fluorescent nanoparticles. As a proof of concept, Eu and Tb doped CaF_2 and LaF_3 NPs were functionalized by aryl diazonium salts bearing $-NO_2$ and -CN groups, using a fast and straightforward protocol based on environmentally friendly reaction conditions, i.e. in water at room temperature and in the presence of air. Although a slight decrease of the fluorescence intensity of the lanthanide-doped fluoride cores was observed after functionalization, probably due to some quenching effect induced by the surface-bound ligands, the bimodal nanoprobes retain intense fluorescence while exhibiting strong SERS signature from the polyaryl shell. Interestingly, the fluorescent and SERS properties of the nanoprobes could be used to track their uptake by cells opening promising prospects for cell labeling and bioimaging applications. Aryl diazonium salt chemistry thus appears as a valuable strategy for the surface functionalization of doped fluoride NPs and the design of bimodal SERS-fluorescence encoded tags.

Supporting Information

The Supporting Information is available: materials, instrumentation, experimental details of synthesis and characterization of different fluoride nanocrystals, functionalization of REDF NPs by aryl diazonium salts, cell culture, cytotoxicity, fluorescence imaging, Raman spectroscopy and imaging and statistical analysis.

Acknowledgements

This research was financially supported by China Scolarship Council (NO. 202006630008). We acknowledge the ImagoSeine core facility of the Institut Jacques Monod, member of the France BioImaging infrastructure (ANR-10-INBS-04) and GIS-IBiSA. We also acknowledge the ITODYS XPS facility (Université Paris Cité, CNRS UMR 7086, PARIS, France). Hydrodynamic diameter studies were performed at the Structural and Molecular Analysis platform core facility of BioMedTech Facilities INSERM US36 | CNRS UAR2009 | Université Paris Cité. This work was supported by the IdEx Université Paris Cité, ANR-18-IDEX-0001 (IVETh plateform), by the Region Ile de France under the convention SESAME 2019 - IVETh (EX047011) (IVETh plateform), by the Region Ile de France and Banque pour l’Investissement (BPI) under the convention Accompagnement et transformation des filières projet de recherche et développement N° DOS0154423/00 & DOS0154424/00 (IVETh platform), and Agence Nationale de la Recherche through the program France 2023 "Integrateur biotherapie-bioproduction" (ANR-22-AIBB-000). We are grateful to Dmitry Ayollo for his help with microscopy experiments and Kelly Aubertin for fruitful discussions. ANR (Agence Nationale de la Recherche) and CGI (Commissariat à l'Investissement d'Avenir) are gratefully acknowledged for their financial support of this work through Labex SEAM (Science and Engineering for Advanced Materials and devices), ANR-10-LABX-096 and ANR-18-IDEX-0001. XPS Spectrometer was also supported by the Ile-de-France regional council, SESAME agreement n°16016303.

References

[1] a) R. A. Alvarez-Puebla, N. Pazos-Perez and L. Guerrini, *Applied Materials Today* **2018**, *13*, 1-14; b) D. A. Heller, S. Baik, T. E. Eurell and M. S. Strano, *Advanced materials* **2005**, *17*, 2793-2799; c) J. Lin, M. E. Graziotto, P. A. Lay and E. J. New, *Cells* **2021**, *10*, 1699-1714.
[2] a) Y. Yue, T. Zhao, Z. Xu, W. Chi, X. Chai, J. Ai, J. Zhang, F. Huo, R. M. Strongin and C. Yin, *Advanced Science* **2023**, *10*, 2205080; b) Z. Li, X. Xia, Y. You, C. Lu, G. Yang, C. Ma, J. Nie, Q. Sun, S. Wu and J. Ren, *Chinese Chemical Letters* **2021**, *32*, 1785-1789; c) W. Zhang, F. Huo, F. Cheng and C. Yin, *Journal of the American Chemical Society* **2020**, *142*, 6324-6331; d) X. Ren, L. Liao, Z. Yang, H. Li, X. Li, Y. Wang, Y. Ye and X. Song, *Chinese Chemical Letters* **2021**, *32*, 1061-1065.
[3] a) F. Nicolson, L. Clark, S. R. Panikkanvalappil, B. Andreiuk and C. Andreou, *Nanotheranostics* **2022**, *6*, 31-49; b) C. Wang, W. Fan, Z. Zhang, Y. Wen, L. Xiong and X. Chen, *Advanced Materials* **2019**, *31*, 1-32.
[4] S. Liu, L. D'Amario, S. Jiang and H. Dau, *Current Opinion in Electrochemistry* **2022**, 101042-101052.
[5] S. M. Fothergill, C. Joyce and F. Xie, *Nanoscale* **2018**, *10*, 20914-20929.
[6] S. Pawar, A. Bhattacharya and A. Nag, *ACS omega* **2019**, *4*, 5983-5990.
[7] M. Kim, J. H. Lee and J. M. Nam, *Advanced Science* **2019**, *6*, 1900471-1900494.
[8] D. Li, K. Aubertin, D. Onidas, P. Nizard, N. Félidj, F. Gazeau, C. Mangeney and Y. Luo, *Wiley Interdisciplinary Reviews: Nanomedicine and Nanobiotechnology* **2022**, *14*, 1-27.
[9] J. Kim, Y. Jang, N.-J. Kim, H. Kim, G.-C. Yi, Y. Shin, M. H. Kim and S. Yoon, *Frontiers in chemistry* **2019**, *7*, 582-589.
[10] L. Cheng, K. Yang, S. Zhang, M. Shao, S. Lee and Z. Liu, *Nano research* **2010**, *3*, 722-732.
[11] Z. Yu, Y. He, T. Schomann, K. Wu, Y. Hao, E. Suidgeest, H. Zhang, C. Eich and L. J. Cruz, *Pharmaceutics* **2022**, *14*, 840-858.
[12] D. Przybylska and T. Grzyb, *Journal of Materials Science* **2020**, *55*, 14166-14178.
[13] M. Tan, B. Del Rosal, Y. Zhang, E. M. Rodríguez, J. Hu, Z. Zhou, R. Fan, D. H. Ortgies, N. Fernández and I. Chaves-Coira, *Nanoscale* **2018**, *10*, 17771-17780.
[14] S. Tiwari, R. Yadav, S. Maurya, A. Kumar, V. Kumar and H. Swart in *Synthesis and Potential*

Application of Rare Earth Doped Fluoride Based Host Matrices, *Vol. 16* CRC Press, **2020**, 16. 240-256.

[15] V. Tikhomirov, M. Mortier, P. Gredin, G. Patriarche, C. Görller-Walrand and V. Moshchalkov, *Optics express* **2008**, *16*, 14544-14549.

[16] J. T. LaBelle, *Design feasibility of a nanoscale biophotonic hybrid device*, Arizona State University, **2001**, 23. 1-24.

[17] D. Cohen, R. Mashiach, L. Houben, A. Galisova, Y. Addadi, D. Kain, A. Lubart, P. Blinder, H. Allouche-Arnon and A. Bar-Shir, *ACS nano* **2021**, *15*, 7563-7574.

[18] a) R. Ahmad, N. Félidj, L. Boubekeur-Lecaque, S. Lau-Truong, S. Gam-Derouich, P. Decorse, A. Lamouri and C. Mangeney, *Chemical Communications* **2015**, *51*, 9678-9681; b) I. Tijunelyte, I. Kherbouche, S. Gam-Derouich, M. Nguyen, N. Lidgi-Guigui, M. L. de la Chapelle, A. Lamouri, G. Lévi, J. Aubard and A. Chevillot-Biraud, *Nanoscale Horizons* **2018**, *3*, 53-57; c) A. Aghajani, M. P. Santoni, P. Mirzaei, A. A. Mohamed, M. M. Chehimi and M. Jouini, *Applied Organometallic Chemistry* **2022**, *36*, 1-12; d) A. A. Mohamed, Z. Salmi, S. A. Dahoumane, A. Mekki, B. Carbonnier and M. M. Chehimi, *Advances in colloid and interface science* **2015**, *225*, 16-36; e) D. Li, Y. Luo, D. Onidas, L. He, M. Jin, F. Gazeau, J. Pinson and C. Mangeney, *Advances in Colloid and Interface Science* **2021**, *294*, 102479-102484; f) M. Bastide, S. Gam-Derouich and J.-C. Lacroix, *Nano Letters* **2022**, *22*, 4253-4259; g) D. Li, P. Nizard, D. Onidas, A. Lamouri, J. Pinson, S. Mahouche-Chergui, K. Aubertin, F. Gazeau, Y. Luo and C. Mangeney, *Nanoscale* **2022**, *14*, 1452-1458.

[19] F. Miller, S. Wintzheimer, T. Reuter, P. Groppe, J. Prieschl, M. Retter and K. Mandel, *ACS Applied Nano Materials* **2019**, *3*, 734-741.

[20] L. Lutterotti, S. Matthies and H. R. Wenk, *IUCr: Newsletter of the CPD* **1999**, *21*, 14-15.

[21] C. d. S. Bezerra and M. E. Valerio, *Physica B: Condensed Matter* **2016**, *501*, 106-112.

[22] a) A. Mesnage, X. Lefèvre, P. Jégou, G. Deniau and S. Palacin, *Langmuir* **2012**, *28*, 11767-11778; b) R. Ahmad, L. Boubekeur-Lecaque, M. Nguyen, S. p. Lau-Truong, A. Lamouri, P. Decorse, A. Galtayries, J. Pinson, N. Felidj and C. Mangeney, *The Journal of Physical Chemistry C* **2014**, *118*, 19098-19105.

[23] P. Doppelt, G. Hallais, J. Pinson, F. Podvorica and S. Verneyre, *Chemistry of Materials* **2007**, *19*, 4570-4575.

[24] a) Y. Zhang, Q. Zhao, B. Shao, W. Lü, X. Dong and H. You, *RSC advances* **2014**, *4*, 35750-35756; b) X. Chen and G. Liu, *Journal of Solid State Chemistry* **2005**, *178*, 419-428; c) W. Chen, Y. Ouyang and M. Mo, *Journal of the American Ceramic Society* **2022**, *105*, 2646-2654.

[25] a) M. Haase and H. Schäfer, *Angewandte Chemie International Edition* **2011**, *50*, 5808-5829; b) S. Han, R. Deng, X. Xie and X. Liu, *Angewandte Chemie International Edition* **2014**, *53*, 11702-11715.

[26] J. Pinson and F. Podvorica, *Chemical Society Reviews* **2005**, *34*, 429-439.

[27] S. Betelu, I. Tijunelyte, L. Boubekeur-Lecaque, I. Ignatiadis, J. Ibrahim, S. Gaboreau, C. Berho, T. Toury, E. Guenin and N. Lidgi-Guigui, *The Journal of Physical Chemistry C* **2016**, *120*, 18158-18166.

[28] M. Hu, Z. Huang, R. Liu, N. Zhou, H. Tang and G. Meng, *Nanoscale Advances* **2022**, *4*, 4730-4738.

[29] D. Hetemi, H. Hazimeh, P. Decorse, A. Galtayries, C. Combellas, F. Kanoufi, J. Pinson and F. I. Podvorica, *Langmuir* **2015**, *31*, 5406-5415.

[30] F. Cavalli, H. Mutlu, S. O. Steinmueller and L. Barner, *Polymer Chemistry* **2017**, *8*, 3778-3782.

[31] B. L. Hurley and R. L. McCreery, *Journal of The Electrochemical Society* **2004**, *151*, B252.
[32] a) S. Sanders and T. D. Golden, *Langmuir* **2019**, *35*, 5841-5847; b) K. Bell, P. Brooksby, M. Polson and A. Downard, *Chemical Communications* **2014**, *50*, 13687-13690; c) K. Brymora, J. Fouineau, A. Eddarir, F. Chau, N. Yaacoub, J.-M. Grenèche, J. Pinson, S. Ammar and F. Calvayrac, *Journal of Nanoparticle Research* **2015**, *17*, 1-9.
[33] S. P. Prakash and K. R. Gopidas, *ChemistrySelect* **2016**, *1*, 4803-4813.

Table of contents entry

Owing to their outstanding photoluminescent properties, lanthanide-doped fluoride nanoparticles such as Eu^{3+} or Tb^{3+} doped CaF_2 and LaF_3 nanoparticles hold huge promise in bioimaging. Herein, these nanoparticles are used for the first time as bimodal fluorescent-Raman probes, thanks to their functionalization by Raman tags using diazonium salts. The resulting bimodal nanoprobes offer unprecedented opportunities for intracellular fluorescence and Raman imaging.

ToC Figure